FTIR and Raman Study of the $Li_xTi_yMn_{1-y}O_2$ (y = 0, 0.11) Cathodes in Methylpropyl Pyrrolidinium Bis(fluoro-sulfonyl)imide, LiTFSI Electrolyte

Laurence J. Hardwick[a,*], Juliette A. Saint[b], Ivan T. Lucas[a,*], Marca M. Doeff[b,*], Robert Kostecki[a,z,*]

[a]Environmental Energy Technologies Division,

[b]Materials Sciences Division,

Lawrence Berkeley National Laboratory,

University of California

Berkeley, CA 94720, USA

[*]Electrochemical Society Active Member

[z]Corresponding author:

email address: r_kostecki@lbl.gov, tel: (1) 510 486 6002, fax: (1) 510 486 7303

Abstract

This work demonstrates the protective effect of partial titanium substitution in $Li_xTi_{0.11}Mn_{0.89}O_2$ against surface decomposition in room temperature ionic liquid (RTILs) cells. Raman microscopy and reflectance FTIR spectroscopy were used to analyze electrodes recovered from cycled $Li/Li_xTi_yMn_{1-y}O_2$ (y = 0, 0.11) cells containing the 0.5 mol/kg LiTFSI in $P_{13}FSI$ RTIL electrolyte. Raman and FTIR spectra of cycled Li_xMnO_2 cathodes showed many distinct bands that can be attributed to both the electrolyte and electrode decomposition products. The thickness of the amorphous porous layer on the Li_xMnO_2 cathode increased during cycling. The surface degradation of Li_xMnO_2 and precipitation of electrolyte decomposition products contributed to the film growth. Improved cycling behavior was observed in cells containing $Li_xTi_{0.11}Mn_{0.89}O_2$, yet Raman spectroscopy also showed possible surface degradation. The FTIR spectra of cycled Li_xMnO_2 and $Li_xTi_{0.11}Mn_{0.89}O_2$ cathodes displayed bands characteristic for $LiSO_3CF_3$ and $Li_2NSO_2CF_3$, which originate from the reaction of the TFSI anion with traces of water present in the cell.

Introduction

Manganese oxide tunnel compounds with the $Na_{0.44}MnO_2$ structure are attractive candidates for use as cathodes in lithium batteries due to the prospective cost savings and their robust nature.[1,2,3,4,5] However, a significant portion of the capacity lies above 4.4 V vs. Li/Li^+, limiting the energy density attainable with conventional electrolytes.[6] Above 4.2 V a substantial increase of interfacial impedance has been reported that results in considerable power loss and arises from the formation of surface films due to electrolyte oxidation and $LiPF_6$ decomposition.[8] Room temperature ionic liquids (RTILs)[7] potentially offer a wider stability window to allow for the complete removal of lithium from all the sites in the tunnel compound. Indeed some classes of RTIL have been shown to be electrochemically stable up to 5.4 V vs. Li/Li^+.[9] Consequently, these materials may be able to reach their theoretical capacity of 193 mAh/g in RTILs, compared to 120 mAh/g typically obtained in ambient temperature conventional electrolytes.

Much attention has been directed to pyrrolidinium-based ionic liquid electrolyte systems due to the good compatibility with metallic lithium.[7,10] Li_xMnO_2 cathodes with the $Na_{0.44}MnO_2$ structure cycle stably in polymer electrolytes or carbonate-based electrolytes at 80°C and room temperature, respectively.[3] However, it exhibits poor cycling behavior in lithium cells with pyrrolidinium-based RTILs.[11] This is caused by a cathode dissolution/precipitation process, evidenced by changes observed in the SEM images and XRD patterns of fresh and cycled electrodes. In contrast, the isostructural $Li_xTi_{0.11}Mn_{0.89}O_2$ material cycles stably and shows no signs of significant degradation.

The goal of this study was to continue previous work[11] in the evaluation of the electrochemical cycling performance of Li_xMnO_2 and $Li_xTi_{0.11}Mn_{0.89}O_2$ cathodes in 0.5 mol/kg LiTFSI in $P_{13}FSI$ electrolyte vs. Li-foil anodes. Formerly these materials showed reasonably stable stability only up to 4.4 V vs. Li/Li^+.[11] Therefore to better understand the processes occurring in cells cycled to both 4.4 V, before cycling to higher potentials are attempted, e*x situ* surface analysis of the anodes and cathodes from cycled cells were carried out by SEM, AFM, and Raman and FTIR spectroscopy.

Experimental

The synthesis of Li_xMnO_2 and $Li_xTi_{0.11}Mn_{0.89}O_2$ ($x \leq 0.44$) is described in reference 2. Composite positive electrodes were prepared by mixing the active material (80%) with carbon black (6%), SFG-6 graphite (TIMCAL SA) (6%) and poly(vinylidene fluoride) (PVDF) Kynar (8%) in N-methylpyrrolidinone (NMP) and doctor-bladed onto a carbon coated aluminum foil (Intelicoat Technologies). Composite cathodes with active material loading between 8 and 15 mg/cm^2 were dried for 24 h at ambient conditions and then for another 24 h at 120 °C under vacuum. Coin cells (2032 size), which consisted of a Li-foil anode, the composite cathode, and Celgard 3401 separator soaked with the solution of 0.5 mol/kg LiTFSI in $P_{13}FSI$ (TFSI= bis(trifluoromethanesulfonyl)imide, P_{13}=methylpropyl pyrrolidinium, and FSI= bis(fluoro-sulfonyl)imide, see Figure 1) were assembled in an Ar-filled glove box. Karl-Fischer titration determined the water content of the samples to be in the range of 20-50 ppm. A MacPile battery cycler (BioLogic SA Claix, France) was used to cycle cells between 2.7 and 4.4 V at current densities

corresponding to ~*C*/15 rate (where *C* is defined as charge or discharge of the full theoretical capacity in one hour).

The cycled coin cells were first fully discharged to 2.7 V then opened and disassembled in the glove box. The surface morphology of the composite Li_xMnO_2 and $Li_xTi_{0.11}Mn_{0.89}O_2$ electrodes were examined with scanning electron microscopy (SEM, model Hitachi S-4300 SE/N). Before SEM analysis, cycled cathodes were washed in dimethyl carbonate (DMC) and dried under vacuum. Raman microscopy (Labram, ISA Groupe Horiba), analysis was carried out in an air-tight cell equipped with a 0.2 mm thick glass window. A laser excitation wavelength of 632.8 nm was used and the laser spot was ca. 1 μm at the surface. The laser power was reduced to ~ 0.8 mW to avoid sample heating. Peak positions and band widths were obtained by fitting with a Lorenztian function.

FTIR measurements of cycled Li_xMnO_2 or $Li_xTi_{0.11}Mn_{0.89}O_2$ cathodes and lithium anodes were conducted in an air-tight spectroscopic cell equipped with a KBr optical window. To avoid a possible interference from DMC or other solvents, FTIR measurements were performed with unwashed electrodes with residual RTIL remaining on the surface. FTIR spectra were recorded on four locations on the electrode surface with the median spectrum reported. The FTIR microscope (Continuμm Nexus 870, Nicolet) equipped with a broadband mercury-cadmium-telluride (MCT) detector was used to collect spectra in the reflectance mode with a resolution of 4 cm^{-1}, using a total of

2880 co-added scans. Spectra were baseline corrected in order to compare the relative absorbance of the surface films, but no smoothing algorithm was used.

An atomic force microscope (AFM, Pico SPM, Molecular Imaging) with an electronic controller (Park Scientific Instruments) was used to study the surface topography of fresh and cycled lithium anodes. The AFM was applied in the constant-force mode with Si triangular cantilevers (Mikromasch). The measurements were conducted in a dry argon atmosphere.

Results and Discussion

Typical galvanostatic cycling and columbic efficiency results for Li/Li_xMnO_2 and Li/$Li_xTi_{0.11}Mn_{0.89}O_2$ cells containing 0.5 mol/kg LiTFSI, P_{13}FSI are shown in Figure 2. While the cell discharge capacity initially rises for both cathodes (most likely due to improved wetting of the electrode by the electrolyte), severe capacity fading (30%) is observed for the Li_xMnO_2 cell after 50 cycles. Interestingly, the Li/$Li_xTi_{0.11}Mn_{0.89}O_2$ cell exhibits much more stable behavior and shows only moderate capacity fading (~6%) after 160 cycles. Both cathodes display only ca. 50% of their theoretical capacity due to a still relatively low voltage limit of 4.4 V and possible kinetic limitations. The rapid degradation of the Li/Li_xMnO_2 cell must arise from specific interactions between the RTIL and the cathode, as Li_xMnO_2 with the $Na_{0.44}MnO_2$ structure cycles extremely well with conventional organic carbonate electrolytes in a similar voltage range.[2,3]

Ex situ AFM images of fresh lithium foil and Li anodes from a cycled Li/Li_xMnO_2 cell are shown in Figure 3. The surface of the fresh Li electrode consists of 200-300 nm densely packed Li domains. The image of the cycled Li anode reveals very similar surface morphology with slightly larger grains packed tightly together. The observed enlargement of Li domains is mainly due to multiple stripping/plating processes during cell cycling. No clear evidence of thick surface films or deposits was observed, which in concert with the stable electrochemical cycling of $Li/Li_xTi_{0.11}Mn_{0.89}O_2$ cells, suggests that the Li anode is not responsible for the electrochemical degradation of the Li/Li_xMnO_2 cell.

A typical FTIR transmission spectrum of the 0.5 mol/kg LiTFSI $P_{13}FSI$ electrolyte and FTIR reflectance spectrum of the lithium anode from a cycled $Li_xMn_{1-y}Ti_yO_2$ cell are shown in Figure 4. All lithium anodes from cells investigated in this study produced nearly identical spectra regardless of cycle number or whether the cathode used was Li_xMnO_2 or $Li_xTi_{0.11}Mn_{0.89}O_2$. The peak assignments for the 0.5 mol/kg LiTFSI $P_{13}FSI$ electrolyte are listed in Table 1.[7,12,13,14,15] The spectra of the electrolyte and the Li anode surface exhibit a similar pattern of bands, although the relative intensities of the peaks vary.

Figure 4c shows the spectrum of Li-anode after subtraction of the signal from the electrolyte. Both spectra were baseline corrected and normalized to the intensity of the most prominent peak of the P_{13} υ_{C-H} stretch at 2979 cm^{-1} prior to subtraction.[7] The P_{13} C-H group band was chosen as reference because it remains unchanged upon exposure to

lithium. Table 2 provides assignments for the peaks that consistently appeared in the Li differential spectrum. Positive peaks in the differential spectrum suggest the presence of new species on the lithium whereas negative peaks imply a loss of the signal from the electrolyte components.

The peak intensity analysis of the differential spectrum of the lithium anode indicates the decrease of bands at 1385, 1361, 1216, 1179, 1105 and 830 cm^{-1}. All these peaks originate from the FSI^- anion. On the other hand, small positive peaks at 1328, 1134 cm^{-1} can be assigned to $TFSI^-$ bands. This suggests that the relative $FSI^-/TFSI^-$ ratio at the lithium surface is much lower than in the bulk electrolyte; i.e., $TFSI^-$ is the dominant anion on the surface of Li anode whereas FSI^- is depleted.

Weak positive bands observed at 1152 and 1238 cm^{-1} suggest the presence of reduction products of $TFSI^-$, such as $CF_3SO_2^-$ at the surface.[7,16] No specific bands could be positively assigned to products of FSI^- reduction, though apart from CF_3 vibrations these products are likely to have bands similar to products of $TFSI^-$ reduction.

Figure 5a and 5b show SEM images of fresh Li_xMnO_2 and $Li_xTi_{0.11}Mn_{0.89}O_2$ electrodes. The needle-like particles of the active material are readily apparent, as well as large flakes of graphite and agglomerates of acetylene black. The SEM image of the cycled $Li_xTi_{0.11}Mn_{0.89}O_2$ cathode shows no changes of surface morphology or evidence of surface deposits (Figure 5d), which is in concert with the improved cycling performance. In contrast to $Li_xTi_{0.11}Mn_{0.89}O_2$, the SEM image of the cycled Li_xMnO_2 electrode reveals

dramatic changes in the surface morphology (Figure 5c). The components of the composite cathode can no longer be distinguished; they appear to be covered with a thick surface film, which is most likely responsible for the observed severe capacity fading. The XRD diffraction pattern of the cycled Li_xMnO_2 electrodes does not indicate the presence of any new phases, but significant broadening of peaks attributable to the Li_xMnO_2 phase was observed.[11] EDX analysis (not shown here) of the Li_xMnO_2 electrode surface and brownish stains on the Celgard separator on the cathode side revealed Mn-containing compounds.

The structure of $Na_{0.44}MnO_2$ consists of edge and corner-sharing MnO_6 octahedra and MnO_5 square pyramids that form two different types of tunnels.[3,17] There are five manganese and three lithium environments; two in the large S-shaped tunnels and one in the smaller pentagonal tunnels.[17] The Raman spectra of Li_xMnO_2 and $Li_xTi_{0.11}Mn_{0.89}O_2$ tunnel compounds (Figure 6) have a similar intricate spectral signature that comprises of at least 18 distinct bands. $Li_xTi_{0.11}Mn_{0.89}O_2$ is isostructural to Li_xMnO_2 and, apparently though band intensities and positions vary slightly, Ti substitution into Mn sites does not greatly affect the crystalline structure symmetry and the Raman spectrum. The bands can be tentatively assigned (Table 3) based on measurements of similar manganese oxide compounds[18] as Mn-O stretching vibrations (542-741 cm^{-1}), and combinations of Mn-O bending and Li-O stretching motions (505-289 cm^{-1}). No bands could be assigned to a pure Ti-O vibration. The major differences between the spectra of $Li_xTi_{0.11}Mn_{0.89}O_2$ compared to Li_xMnO_2 are the intensity increase of the band at 572 cm^{-1} and the

broadening of the band at 640 cm^{-1}. These could be attributed to Ti substitution in the lattice as the bands occur in the region of titanium oxide compound vibrations.

Raman spectra of cycled Li_xMnO_2 (50 cycles) and $Li_xTi_{0.11}Mn_{0.89}O_2$ (163 cycles) cathodes are shown in Figure 7. The Raman spectrum of the tested Li_xMnO_2 cathode reveals substantial differences in the spectral characteristics. The poorly resolved bands are grouped into two large maxima centered at ca. 650 and 500 cm^{-1}. The exact nature of this manganese oxide layer is difficult to establish, however the Raman peak at 650 cm^{-1} suggests the presence of Mn_3O_4 and bands at 485 and 626 cm^{-1} indicate $Li_xMn_2O_4$ type compounds.[18,19] However, the broad and weak Raman Mn-O contributing bands indicate an amorphous and/or non-stoichiometric character of these manganese oxide compounds that contribute to the surface layer formed on the Li_xMnO_2 electrode during cycling. These results strongly suggest that Li_xMnO_2 undergoes partial surface decomposition and phase transformation during prolonged cycling of Li_xMnO_2 in 0.5 mol/kg LiTFSI in $P_{13}FSI$ to form a highly disordered and non-stoichiometric layer of MnO_x-type products. The spectrum of the cycled $Li_xTi_{0.11}Mn_{0.89}O_2$ cathode also exhibits some differences when compared to the fresh powder. Its spectrum also has bands centered at ca. 650 and 500 cm^{-1}, however these maxima are better resolved and display several of distinct bands of the uncycled material, albeit at much lower signal to noise ratio. In particular, the previously most intense Raman band at 572 cm^{-1} has been reduced to a shoulder band and the most defined peaks can be seen at 510, 611 and 689 cm^{-1}. This spectrum suggests that the surface has reverted to a spinel-like phase, though with limited adverse affect on the electrochemical performance.

Baseline corrected FTIR reflectance spectra of the fresh and cycled Li_xMnO_2 (Figure 8) display numerous peaks that increase substantially in intensity with cycling. Despite the presence of residual RTIL on the surface of the unwashed cathode, spectra measured at various points on the surface, consistently displayed increasing peak intensity with cycle number. These bands correspond to the vibration modes of the electrolyte components and their decomposition products. No spectral response of the cathode active material could be examined because it falls below the limits of the IR detector used in this work.

After one charge/discharge cycle, the peaks assigned to $TFSI^-$ appear altered; most strikingly, the υ_aS-N-S (1058 cm^{-1}) band is absent.[7] New weak peaks associated with $LiSO_3CF_3$ emerge at 1298, 1250 and 1160 cm^{-1} [20,21,22] and the υSO_2 band of $Li_2NSO_2CF_3$ is located at 1335 cm^{-1}.[7] Bands specifically associated with $TFSI^-$ are still observed at 1224 and 1125 cm^{-1}, though similar bands may also originate from reaction products.

The FTIR spectrum of the Li_xMnO_2 cathode after 15 cycles exhibit peaks characteristic for TFSI (υ_aS-N-S 1058 cm^{-1}) and FSI (υ_aS-N-S at 842 cm^{-1}) anions.[14,15] Other distinctive group of bands for SO_2 and CF_3 functionalities in $TFSI^-$ and FSI^- are observed at 1369, 1335, 1225, 1205, 1152 and 1119 cm^{-1}. The intense broad peak from 1340 to 1200 cm^{-1} is likely to contain contributions from $TFSI^-$, FSI^-, $LiSO_3CF_3$ and $Li_2NSO_2CF_3$. Bands at 975 (υ_1, A_1) and 933 cm^{-1} (υ_3, E) suggest the presence of SO_3^{2-}

species from other anion decomposition products.[25,26] These bands overlap with similar peaks of the P_{13} ring breathing vibrations, but are relatively weak in comparison to other bands of the RTIL (Figure 4). Bands assigned to υ_{C-H} of P_{13} at 2985 and 2890 cm^{-1} and to δ_{C-H} at 1402 cm^{-1} also increase in intensity as cycling progresses. The relative peak intensity remains the same, suggesting that the P_{13}^{+} cation is stable against the Li_xMnO_2/carbon composite electrode within the cycling range of 2.5 and 4.4 V. The spectrum of the Li_xMnO_2 cathode after 50 cycles exhibits a similar spectral pattern, however, the intensity of all bands are practically tripled.

Ying et al.[23] demonstrated the reactivity N-fluoro-bis[(perfluoroalkyl)sulfonyl] imide with water. In polar solvents, water becomes a good nucleophile to attack the sulfonyl group in $TFSI^-$. Our tentative mechanism for the breakdown of $TFSI^-$ occurs by first oxidation of the $TFSI^-$ and then nucleophilic substitution reaction with water to form $LiSO_3CF_3$ and $Li_2NSO_2CF_3$. Trace water is known to originate from cell components, primarily from the carbon additives. Indeed, Kerlau et al.[24] showed that even after three days of drying under vacuum at 120^oC, traces of water were still present in composite cathodes, which reacted with the electrolyte to form a surface film.

Interestingly, the FTIR spectra of the $Li_xTi_{0.11}Mn_{0.89}O_2$ cathode show only very weak υ_{C-H} bands at ca. 2968 and 2877 cm^{-1}, and no other distinct features could be detected from the $Li_xTi_{0.11}Mn_{0.89}O_2$ electrode that was cycled for less than 25 times. The FTIR spectrum of the $Li_xTi_{0.11}Mn_{0.89}O_2$ cathode after 50 cycles (Figure 9) resembles the spectrum of the Li_xMnO_2. However, bands attributed to the electrolyte and its

decomposition products are twice as intense for Li_xMnO_2 as for $Li_xTi_{0.11}Mn_{0.89}O_2$ (Table 4). Moreover, the intensity of the bands $Li_xTi_{0.11}Mn_{0.89}O_2$ after 163 cycles increases only slightly in comparison to 50 cycles, but they do not reach the intensity observed for Li_xMnO_2 after 50 cycles.

These results suggest two main degradation mechanisms that contribute to the surface film growth at the Li_xMnO_2 cathode during prolonged cycling in 0.5 mol/kg LiTFSI in $P_{13}FSI$: (i) surface decomposition and phase transformation of Li_xMnO_2, (ii) direct oxidation of the electrolyte at the cathode accompanied by reactions with water contaminants absorbed in the electrode components. Due to the chemical instability of the Li_xMnO_2/RTIL interface, it is very likely that the surface film undergoes constant reformation on newly formed MnO_x phases, which may also further catalyze oxidation of the electrolyte. The continuous growth of the surface film eventually leads to formation of electronic and ionic barriers within the composite cathode, as well as loss of active material and charge capacity.

The thinner films observed on $Li_xTi_{0.11}Mn_{0.89}O_2$ do not create significant kinetic and/or transport barriers for cathode's electrochemical performance, nor does active material appear to be consumed by side reactions.

Conclusions

Li_xMnO_2 cathodes exhibit poor cycling behavior in coin cells with the Li anode and the 0.5 mol/kg LiTFSI $P_{13}FSI$ RTIL electrolyte in contrast to cells with conventional or polymer electrolytes. Surface decomposition and phase transformation of part of the Li_xMnO_2, and direct oxidation of the electrolyte at the cathode, accompanied by reactions with water contaminants are responsible for the formation of a thick surface film. This complex surface layer creates electronic and ionic barriers within the composite cathode and affects the rate capability and charge capacity.

In contrast, the isostructural $Li_xTi_{0.11}Mn_{0.89}O_2$ material cycles stably, yet shows signs of surface structural change from Raman results. Thin films observed on cycled $Li_xTi_{0.11}Mn_{0.89}O_2$ cathodes consist of electrolyte decomposition products such as $LiSO_3CF_3$ and $Li_2NSO_2CF_3$ that arise from the reaction of $TFSI^-$ with trace water from cell components, but do not appear to affect the electrochemical behavior substantially.

Acknowledgments

This work was supported by the Assistant Secretary for Energy Efficiency and Renewable Energy, Office of FreedomCAR and Vehicle Technologies of the U.S. Department of Energy under Contract No. DE-AC02-05CH11231. We thank Dr. K. Zaghib (Hydro-Quebec, Canada) and Dr. T. Hollenkamp (CSIRO, Australia) for the samples of $P_{13}FSI$.

References

1. M.M. Doeff, T.J. Richardson, L. Kepley, *J. Electrochem. Soc*., **143**, 2507 (1996).
2. J.A. Saint, M.M. Doeff, J. Wilcox, *Chem Mater*, **20**, 3403 (2008).
3. M.M. Doeff, A. Anapolsky, L. Edman, T.J. Richardson, L.C. De Jonghe, *J. Electrochem. Soc*., **148**, 230 (2000).
4. M.M. Doeff, T.J. Richardson, K.-T. Hwang, *J. Power Sources,* **135**, 240 (2004).
5. A.R. Armstrong, H. Huang, R.A. Jennings, P.G. Bruce, *J. Mater. Chem*. **8**, 255 (1998).
6. J. Akimoto, J. Awaka, Y. Takahashi, N. Kijama, M. Tabuchi, A. Nakashima, H. Sakaebe, K. Tatsumi, *Electrochem. Solid State Lett*., **8**, A554 (2005).
7. P.C. Howlett, N. Brack, A.F. Hollenkamp, M. Forsyth, D.R. MacFarlane, *J. Electrochem. Soc*., **153**, A595 (2006).
8. J. Vetter, P. Novák, M.R. Wagner, C. Veit, K.-C. Mller, J.O. Besenhard, M. Winter, M. Wohlfahrt-Mehrens, C. Vogler, A. Hammouche, *J. Power Sources*, **147**, 269 (2005).
9. M. Galiński, A. Lewandowski, I. Stępniak, *Electrochim. Acta*, **51**, 5567 (2006).
10. P.C. Howlett, D.R. MacFarlane, A.F. Hollenkamp, *Electrochem. Solid-State Lett*., **7**, 97 (2004).
11. J. Saint, A.S. Best, A.F. Hollenkamp, J. Kerr, J.-H. Shin, M.M. Doeff, *J. Electrochem. Soc*., **155**, A127 (2008).
12. J. Kiefer, J. Friers, A. Leipertz, *Appl. Spectrosc*., **61**, 1306 (2007).
13. I. Rey, P. Johansson, J. Lindgren, J.C. Lassègues, J. Grondin, L. Servant, *J. Phys. Chem. A, 102*, 3249 (1998).

14. J.K. Ruff, *Inorg. Chem*., **4**, 1446 (1965).

15. J.F. Sawyer, G.J. Schrobilgen, S.J. Sutherland, *Inorg. Chem*., **21**, 4064 (1982).

16. D. Aurbach, I Weissman, A. Zaban, O. Chusid, *Electrochim. Acta*, **39**, 51 (1994).

17. W.G. Mumme, *Acta Crystallogr., Sect. B: Struct. Crystallogr. Cryst. Chem*., **24**, 114 (1968).

18. B. Banov, A. Momchilov, M. Massot, C.M. Julien, *Mater Sci Eng B*, **100**, 87 (2003).

19. F. Buciuman, F. Patcas, R. Cracium, D.R.T. Zahn, *Phys. Chem. Chem. Phys*., **1**, 185 (1999).

20. C.M. Burba, R. Frech, B. Grady, *Electrochim. Acta*, **53**, 1548 (2007).

21. W. Huang, R.A. Wheeler, R. Frech, *Spectrochim. Acta*, **50A**, 985 (1994).

22. R. Frech, *Macromolecules*, **33**, 9432 (2000).

23. W. Ying, D.D. DesMarteau, Z-Q. Xu, M. Witz, *J. Fluorine Chem*., **102**, 135 (2000).

24. M. Kerlau, R. Kostecki, *J. Electrochem. Soc*., **153**, A1644 (2006).

25. K. Nakamoto, *Infrared and Raman Spectra of Inorganic and Coordination Compounds*, Wiley-Interscience, New York (1997).

26. L. Peter, B. Meyer, *Inorg. Chem*., **24**, 3071 (1985).

Table 1: FTIR band positions and assignments for 0.5 mol/kg LiTFSI, $P_{13}FSI$

0.5 mol/kg LiTFSI, $P_{13}FSI$ Band position/ cm^{-1}	**Ref [7]/ cm^{-1}**	**Ref [12]/ cm^{-1}**	**Ref [13]/ cm^{-1}**	**Ref [14]/ cm^{-1}**	**Ref [15]/ cm^{-1}**	**Assignment**
3046w	3041					υCH_2 P_{13}
2979m	2981					υCH_2 P_{13}
2944m	2949					υCH_2 P_{13}
2918m						υCH_2 P_{13}
2887m	2890					υCH_2 P_{13}
2852w						υCH_2 P_{13}
1473m	1470					δCH_2, CH_3 P_{13}
1432w	1434					δCH_2 P_{13}
1384s				1406	1370	$\upsilon_a SO_2$ i FSI
1364sh	1354	1348	1354			$\upsilon_a SO_2$ o FSI and $\upsilon_a SO_2$ i TFSI
1334sh	1335	1331	1334			$\upsilon_a SO_2$ o TFSI
1227sh	1234	1227	1227			υ_s CF_3 TFSI
1217s				1221	1217	$\upsilon_s SO_2$ i FSI
1180m	1193	1200	1195	1190	1174	$\upsilon_a CF_3$ TFSI and $\upsilon_s SO_2$ o FSI
1138w	1139	1132	1136			$\upsilon_s SO_2$ TFSI
1106s				1110		FSI
1058m	1057	1051	1060			υ_aSNS TFSI
		1038				υSO TFSI
1001w	1004					
970w	970					Ring mode P_{13}
936m	939					Ring mode P_{13}
	905					Ring mode P_{13}
	887					Ring mode P_{13}
835s				835	837	υS-F and υ_aSNS FSI
791sh	790	789	788			υC-S TFSI
	762	762	761			υ_sSNS TFSI
				750		
	743	741	739			δCF_3 TFSI
				734	734	υ_sSNS FSI

Table 2: Positions and assignments for the most prominent positive and negative peaks in the differential spectrum for the Li anode after 50 cycles in 0.5 mol/kg LiTFSI, $P_{13}FSI$.

Pos. Peak/ cm^{-1}	**Assignment**
1480	δCH_2, CH_3 P_{13}
1430	δCH_2 P_{13}
1405	$\upsilon_a SO_2$ i FSI
1328	$\upsilon_a SO_2$ o TFSI
1238	$\upsilon_s CF_3$ CF_3SO_2 or TFSI
1152	$\upsilon_a CF_3$ CF_3SO_2
1134	$\upsilon_s SO_2$ TFSI
999	
970	Ring mode
939	Ring mode
895	Ring mode
Neg. peak/ cm^{-1}	**Assignment**
1385	$\upsilon_a SO_2$ i FSI
1361	$\upsilon_a SO_2$ o FSI
1216	$\upsilon_s SO_2$ i FSI
1179	$\upsilon_s SO_2$ o FSI
1105	FSI
830	υS-F and υ_aSNS FSI

Table 3: Raman band positions and FWHM of Li_xMnO_2 and $Li_xTi_{0.11}Mn_{0.89}O_2$ powders.

Li_xMnO_2			**$LiTi_{0.11}Mn_{0.89}O_2$**		
Band Position/ cm^{-1}	**FWHM/ cm^{-1}**	**Assignment**	**Band Position/ cm^{-1}**	**FWHM/ cm^{-1}**	**Assignment**
206	20	υLi-O and δMn-O	205	18	υLi-O, δMn-O and δTi-O
224	12		225	12	
254	5		255	10	
289	28		288	26	
327	21		331	15	
345	10		345	10	
400	11		397	8	
413	12				
440	18		439	24	
480	37		484	33	
504	16		505	21	
539	13	υMn-O	539	17	υMn-O and υTi-O
573	31		572	30	
607	23		607	22	
638	18		640	46	
654	34		658	29	
678	21		678	29	
742	13		742	23	

Table 4: FTIR band positions and assignments of Li_xMnO_2 after 1 and 50 cycles and $Li_xTi_{0.11}Mn_{0.89}O_2$ after 50 cycles in 0.5 mol/kg LiTFSI, $P_{13}FSI$.

Cycled electrode Li_xMnO_2 1 cycle, band position/ cm^{-1}	**Cycled electrode Li_xMnO_2 50 cycles, band position/ cm^{-1}**	**Cycled electrode $Li_xTi_{0.11}Mn_{0.89}O_2$ 50 cycles Band position/ cm^{-1}**	**Assignment**
	3042w	3040w	υCH_2 P_{13}
2980w	2988w	2982w	υCH_2 P_{13}
	2945w	2950w	υCH_2 P_{13}
	2912w	2911w	υCH_2 P_{13}
2888w	2888w	2887w	υCH_2 P_{13}
		2851w	υCH_2 P_{13}
1482w	1485m	1480m	δCH_2, CH_3 P_{13}
1449w	1427m	1432m	δCH_2 P_{13}
1405w	1401w	1398w	$\upsilon_a SO_2$ i FSI
1370w	1369sh	1369sh	$\upsilon_a SO_2$ o FSI and $\upsilon_a SO_2$ i TFSI
1347w			
1333w		1332s	$\upsilon_a SO_2$ o TFSI or $Li_2NSO_2CF_3$
1298w			$\upsilon_a SO_3$ $LiSO_3CF_3$
1250sh			$\upsilon_a SO_3$ $LiSO_3CF_3$
1224m	1225br	1221br	υ_s CF_3 TFSI
1206m	1205s	1201s	$\upsilon_s SO_2$ o FSI, $\upsilon_a CF_3$ TFSI
1160m		1160m	$\upsilon_a CF_3$ $LiSO_3CF_3$
1141sh	1145	1139sh	υ_s SO_2 TFSI
1125sh	1119s	1119m	
	1080sh		
	1065m	1063m	υ_aSNS TFSI
	1009m	1007m	
968w	977m	971m	Ring mode P_{13} or SO_3^{2-}
	945m	939m	Ring mode P_{13} or SO_3^{2-}
914w	900m	910m	Ring mode P_{13}
		883w	Ring mode P_{13}
844m	842m	840m	υS-F and υ_aSNS FSI
774m	769m	765m	C-S

Figure Captions

Figure 1: Molecular structure of $TFSI^-$ (a), FSI^- (b) and P_{13}^+ (c).

Figure 2: Discharge capacity (a) and coulombic efficiency (b) between 4.4 and 2.7 V at *C*/15 rate as a function of cycle number for Li/0.5 mol/kg LiTFSI, $P_{13}FSI/Li_xMnO_2$ and Li/0.5 mol/kg LiTFSI, $P_{13}FSI/Li_xTi_{0.11}Mn_{0.89}O_2$ cells at room temperature.

Figure 3: 5x5 μm AFM images of fresh lithium foil (a), and Li anode from Li/Li_xMnO_2 cell after 50 cycles (b).

Figure 4: FTIR transmission spectrum of 0.5 mol/kg LiTFSI in $P_{13}FSI$ electrolyte (a) and reflectance spectrum of Li-anode from cycled Li/0.5 mol/kg LiTFSI, $P_{13}FSI/Li_xTi_{0.11}Mn_{0.89}O_2$ cell (b). Differential FTIR spectrum of Li-anode after subtraction of the signal from the electrolyte (c). The spectra have been normalized with respect to the P_{13} υ_{C-H} at 2979 cm^{-1}.

Figure 5: SEM images of fresh Li_xMnO_2 (a), $Li_xTi_{0.11}Mn_{0.89}O_2$ (b) electrodes, and Li_xMnO_2 after 40 cycles (c), and $Li_xTi_{0.11}Mn_{0.89}O_2$ after 163 cycles (d) in 0.5 mol/kg LiTFSI $P_{13}FSI$ at room temperature.

Figure 6: Raman spectra of fresh Li_xMnO_2 (a), and $Li_xTi_{0.11}Mn_{0.89}O_2$ (b) powders.

Figure 7: Raman spectra of Li_xMnO_2 electrode after 50 cycles (a) and $Li_xTi_{0.11}Mn_{0.89}O_2$ after 163 cycles (b) in 0.5 mol/kg LiTFSI $P_{13}FSI$ at room temperature.

Figure 8: Reflectance FTIR spectra of Li_xMnO_2 cathode after 1, 15 and 50 cycles in 0.5 mol/kg LiTFSI, $P_{13}FSI$ (a). The insert shows the exploded view of the υ_{C-H} region of the spectra. Transmission spectrum of the 0.5 mol/kg LiTFSI, $P_{13}FSI$ electrolyte (b). The arrows highlight the υ_aSNS TFSI band at ca. 1060 cm^{-1}.

Figure 9: Reflectance FTIR spectra of Li_xMnO_2 (thin line) and $Li_xTi_{0.11}Mn_{0.89}O_2$ (bold line) after 50 cycles.

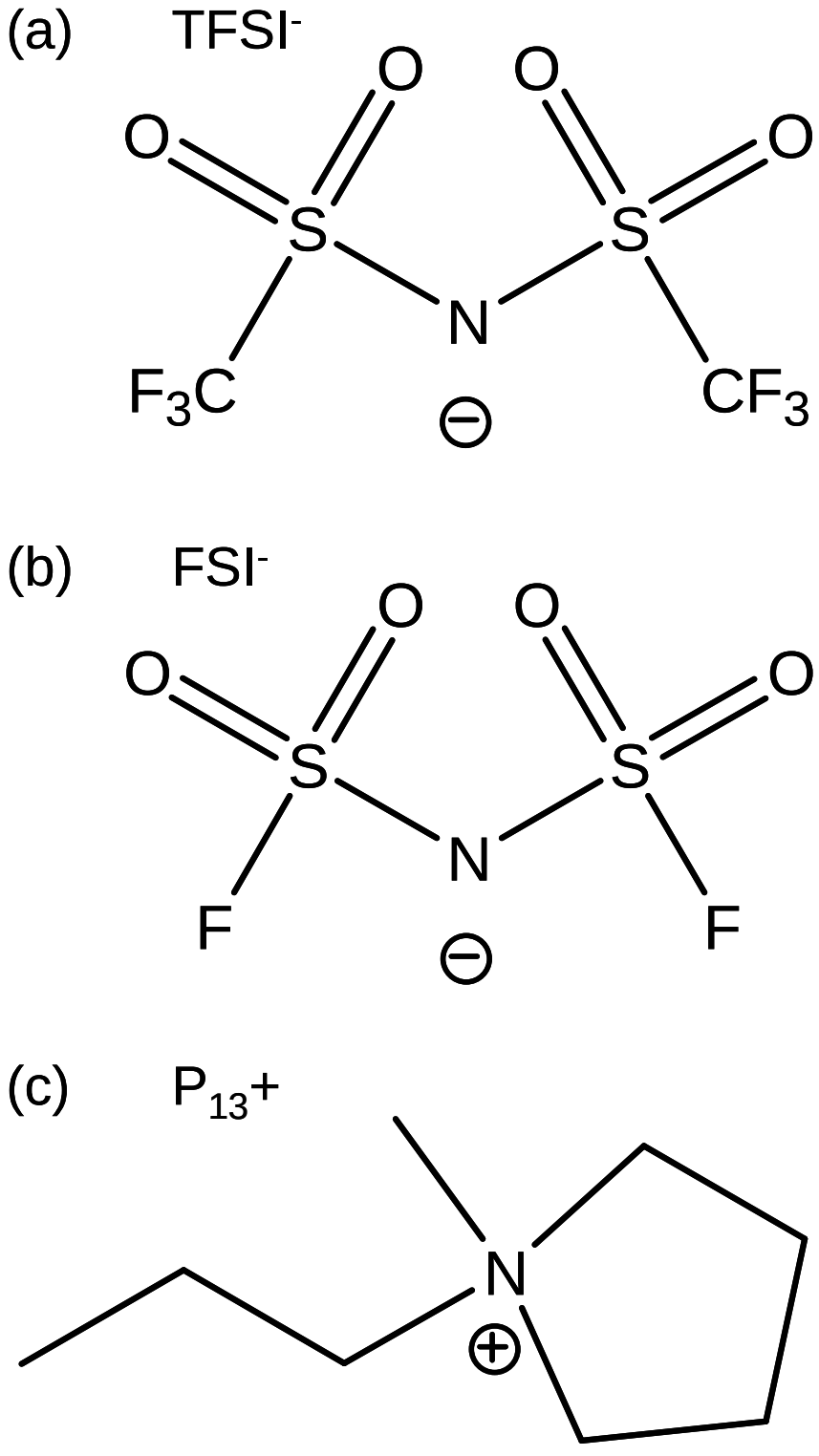

Figure 1: Hardwick et al.

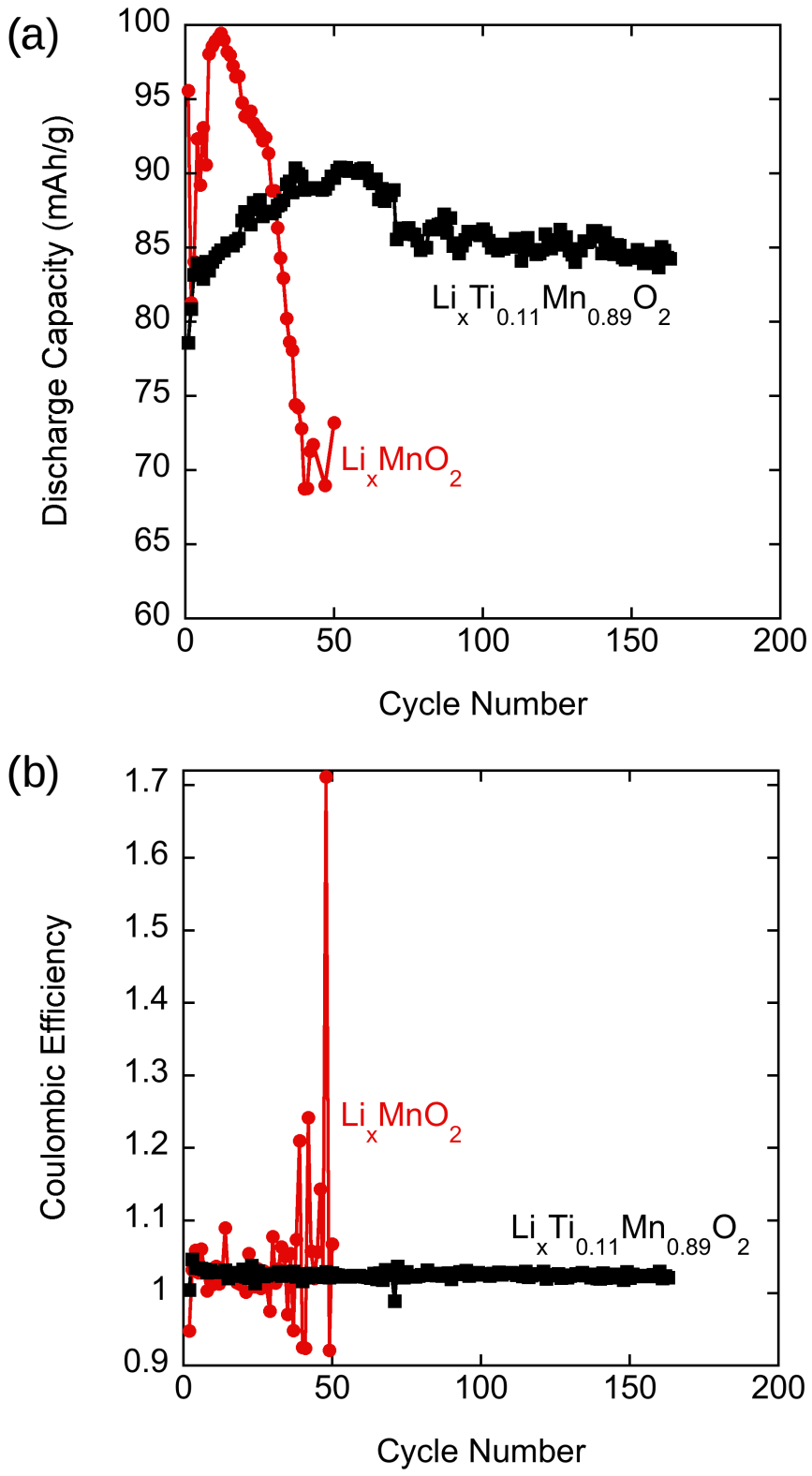

Figure 2: Hardwick et al.

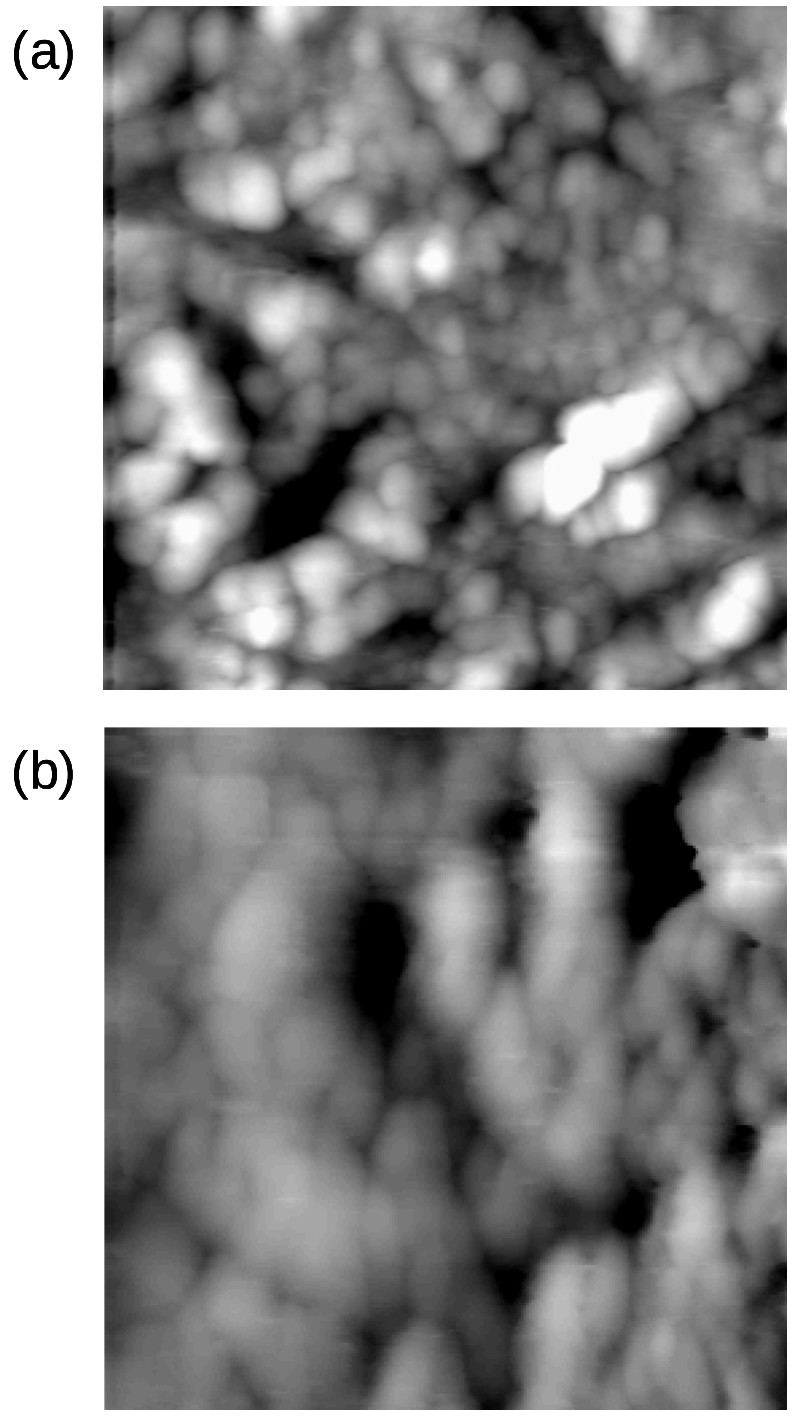

Figure 3: Hardwick et al. (print figure)

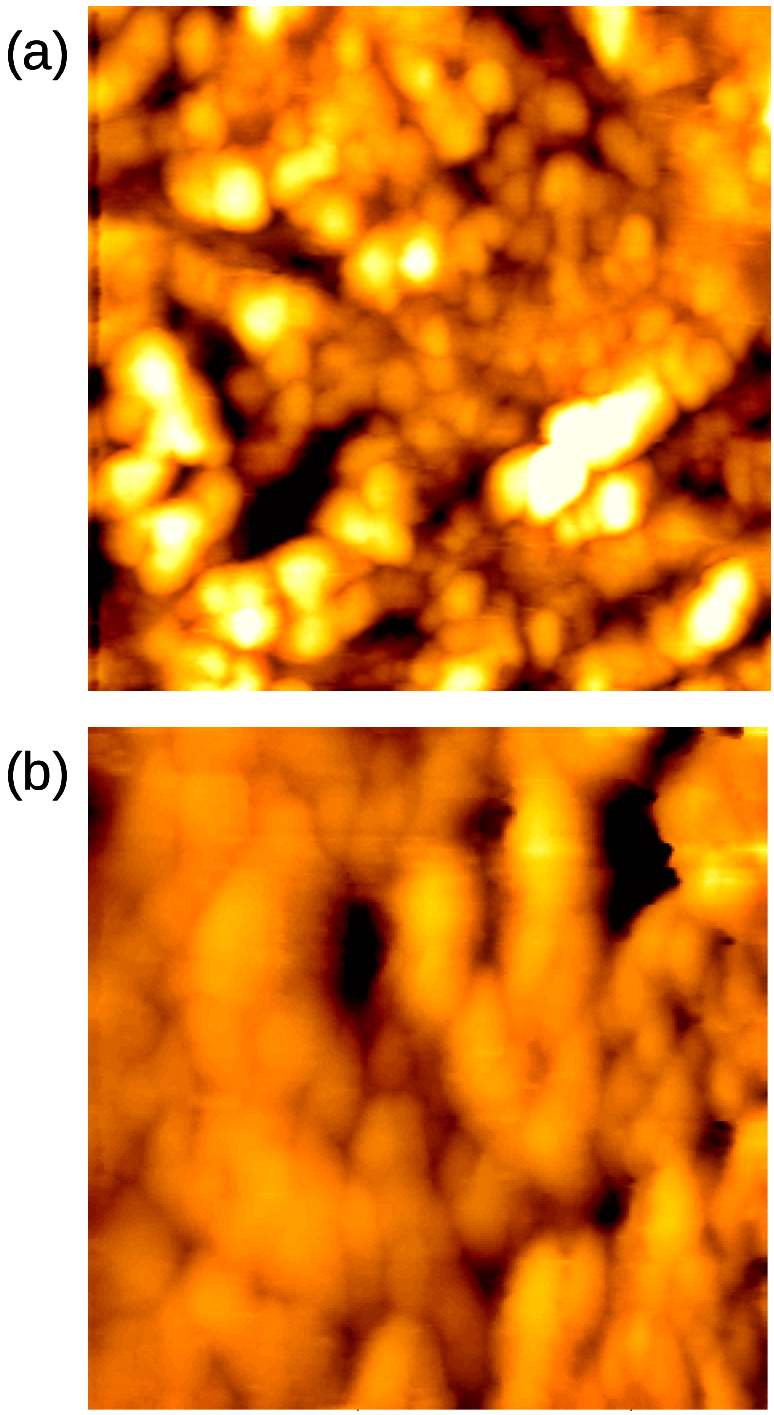

Figure 3: Hardwick et al. (color online figure)

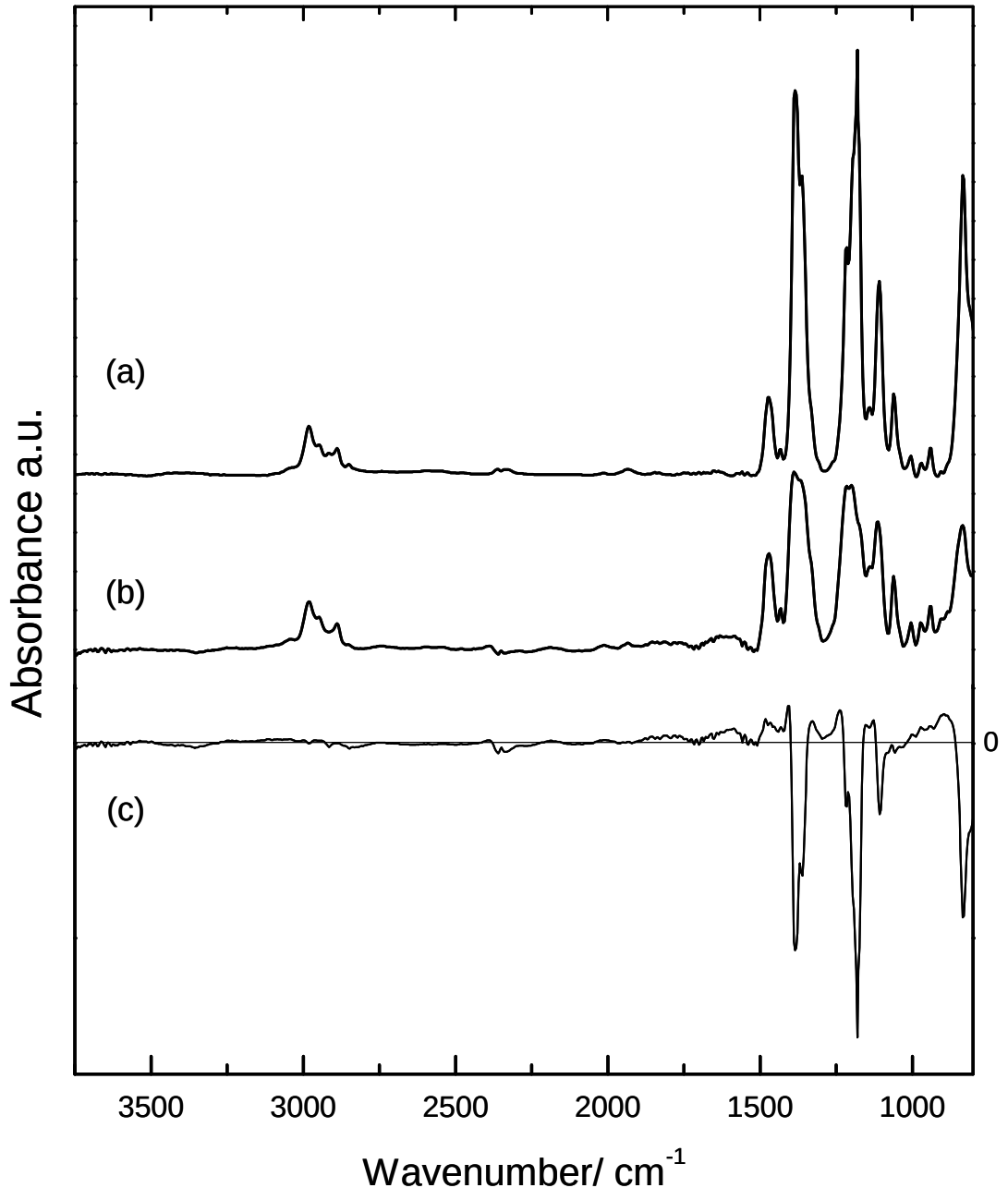

Figure 4: Hardwick et al.

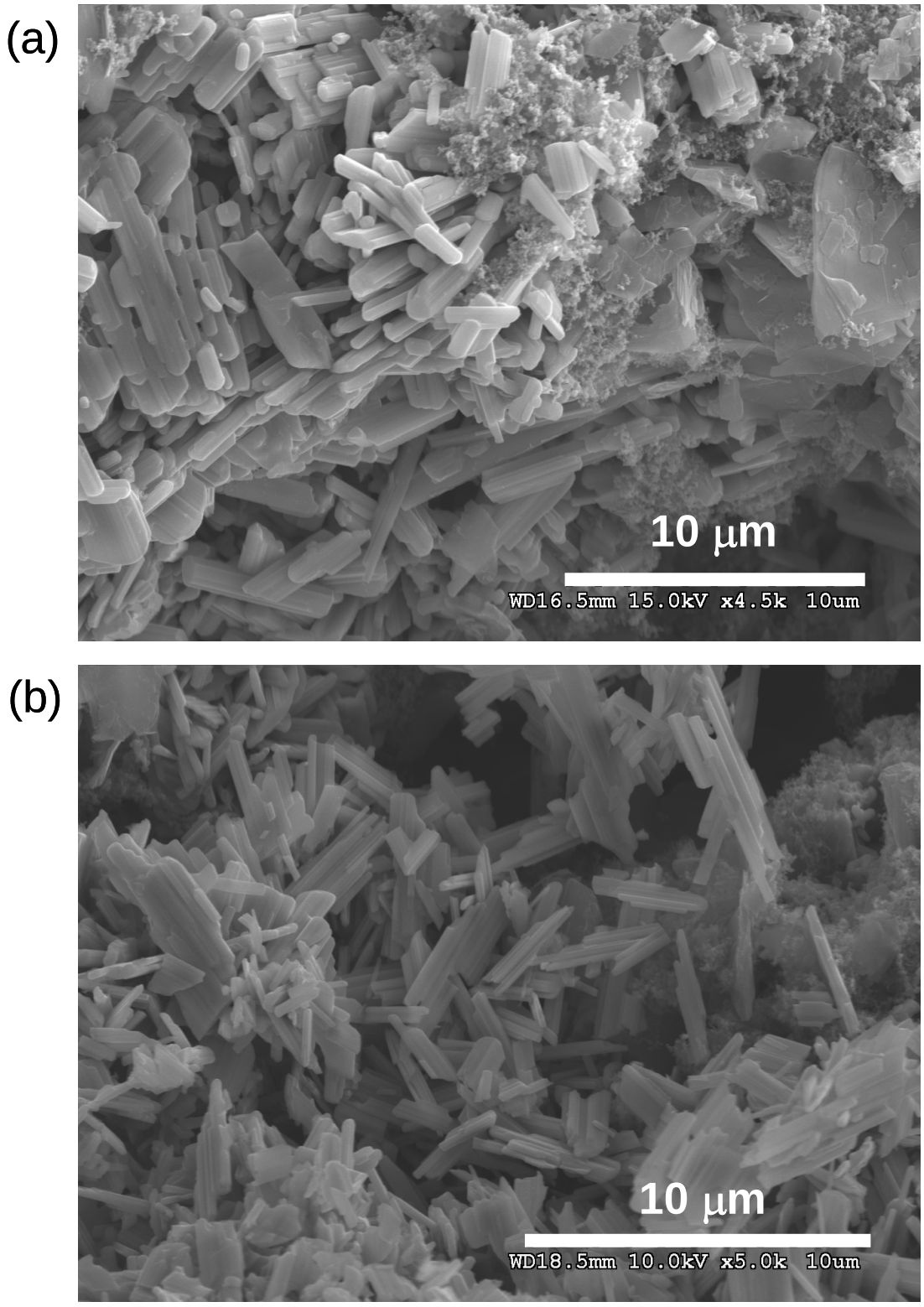

Figure 5: Hardwick et al.

(c)

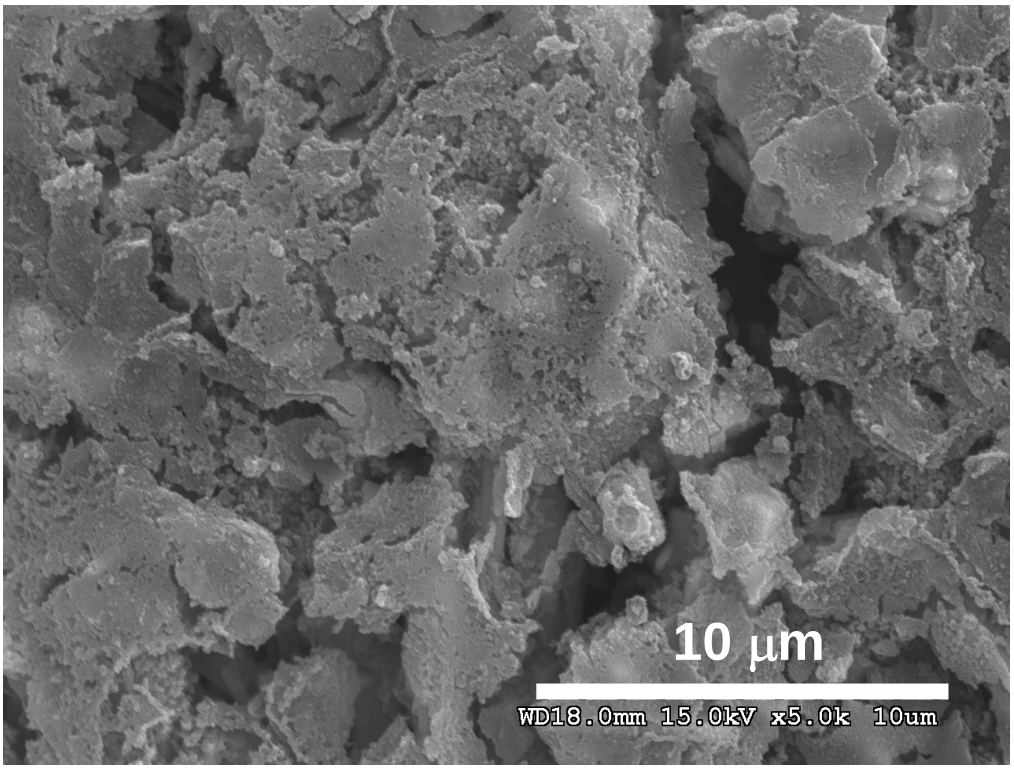

(d)

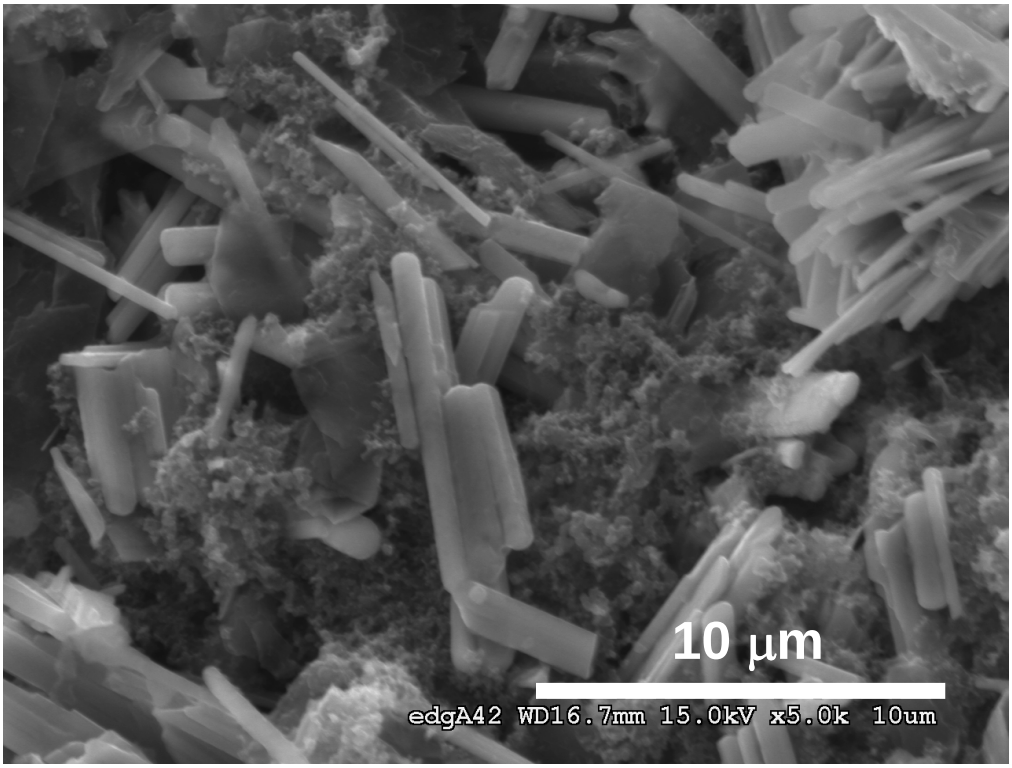

Figure 5 continued: Hardwick et al.

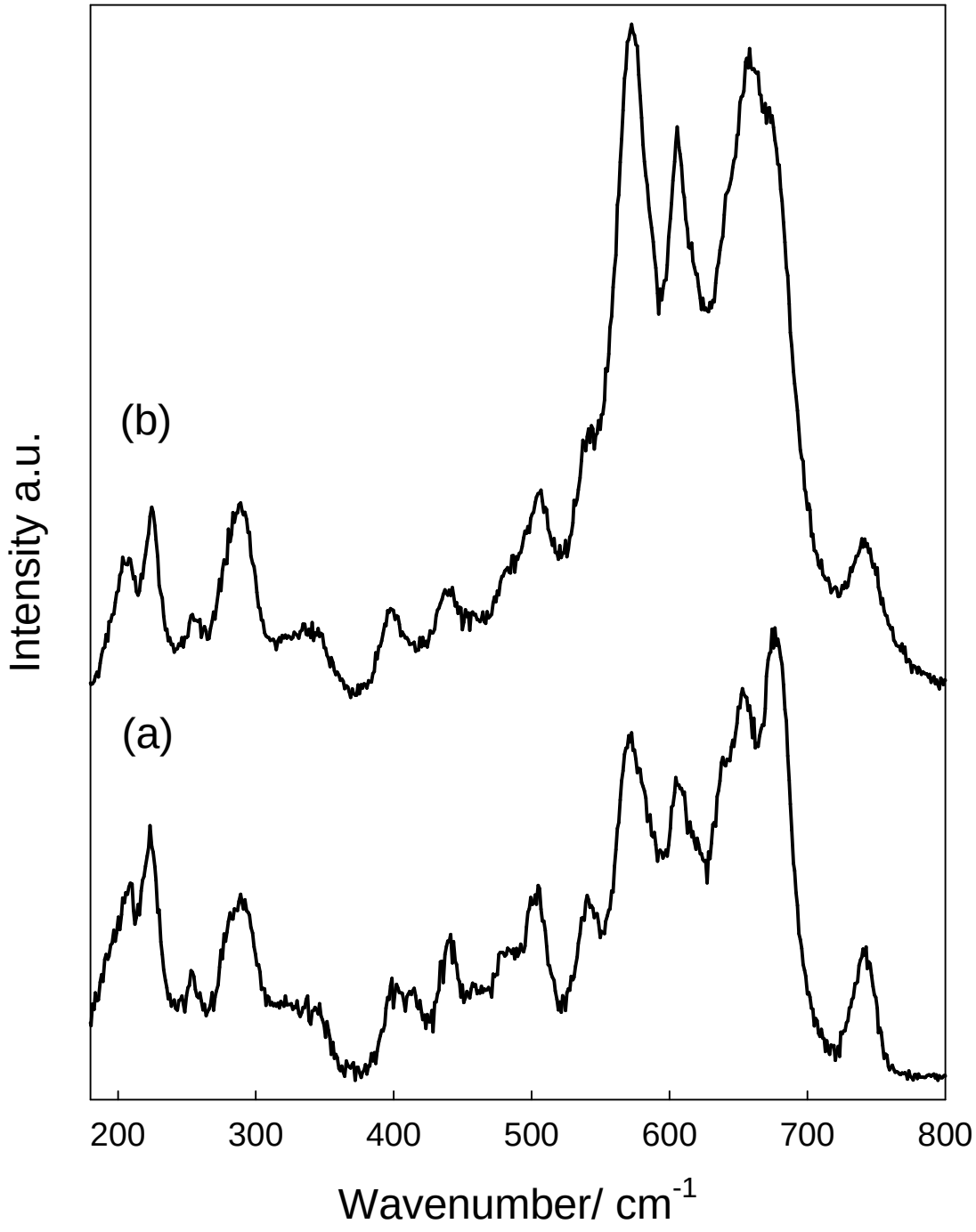

Figure 6: Hardwick et al.

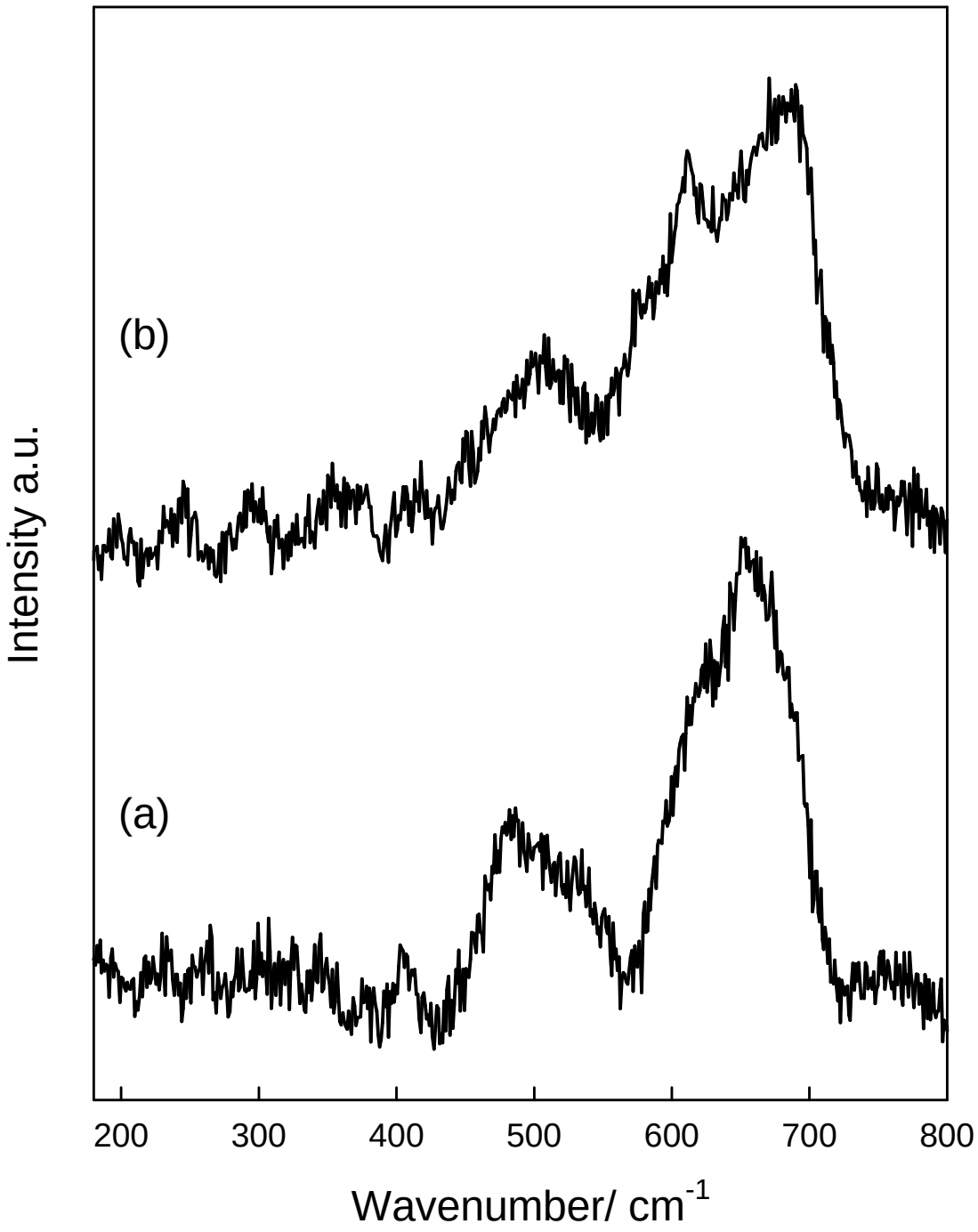

Figure 7: Hardwick et al.

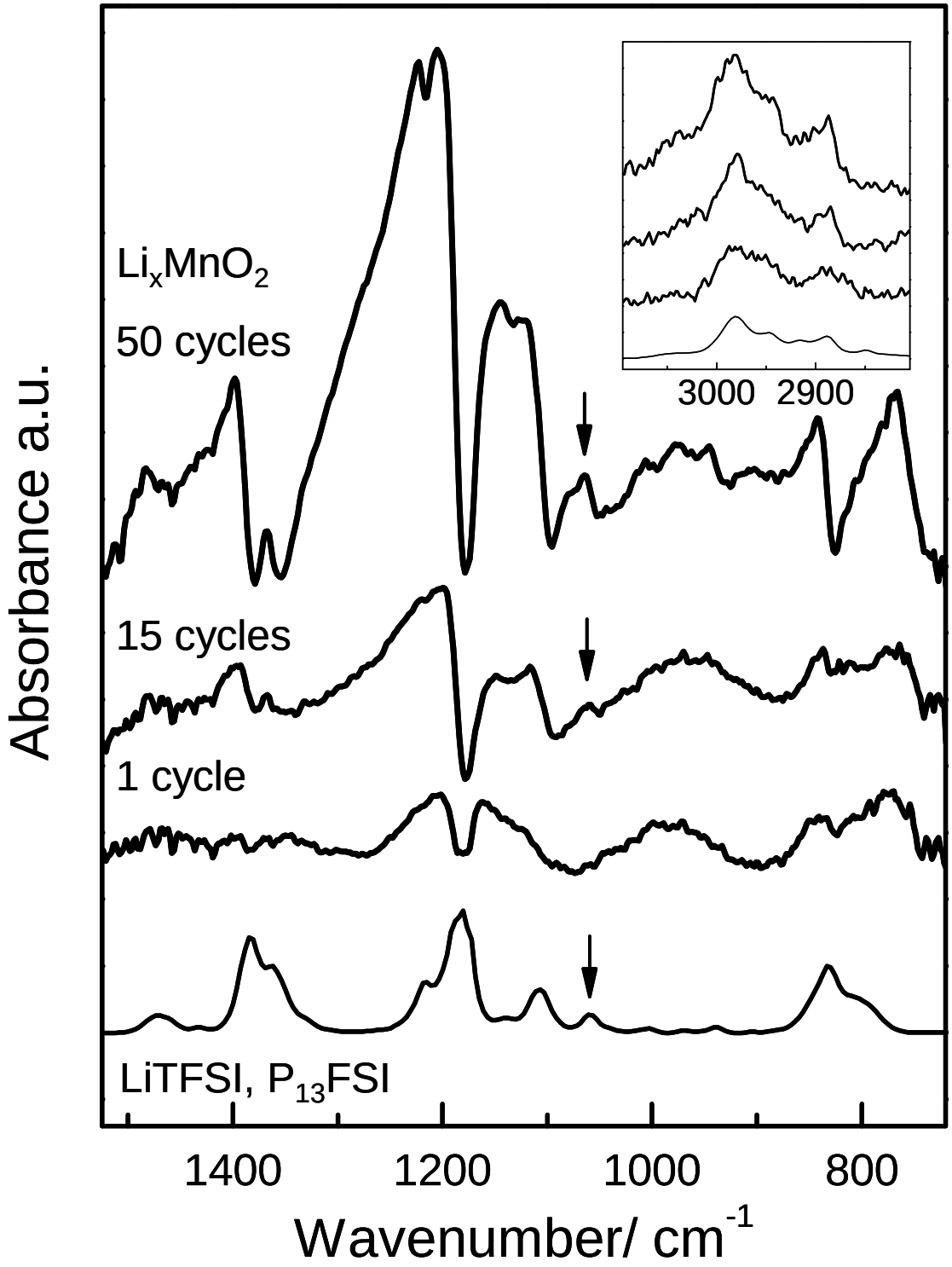

Figure 8: Hardwick et al.

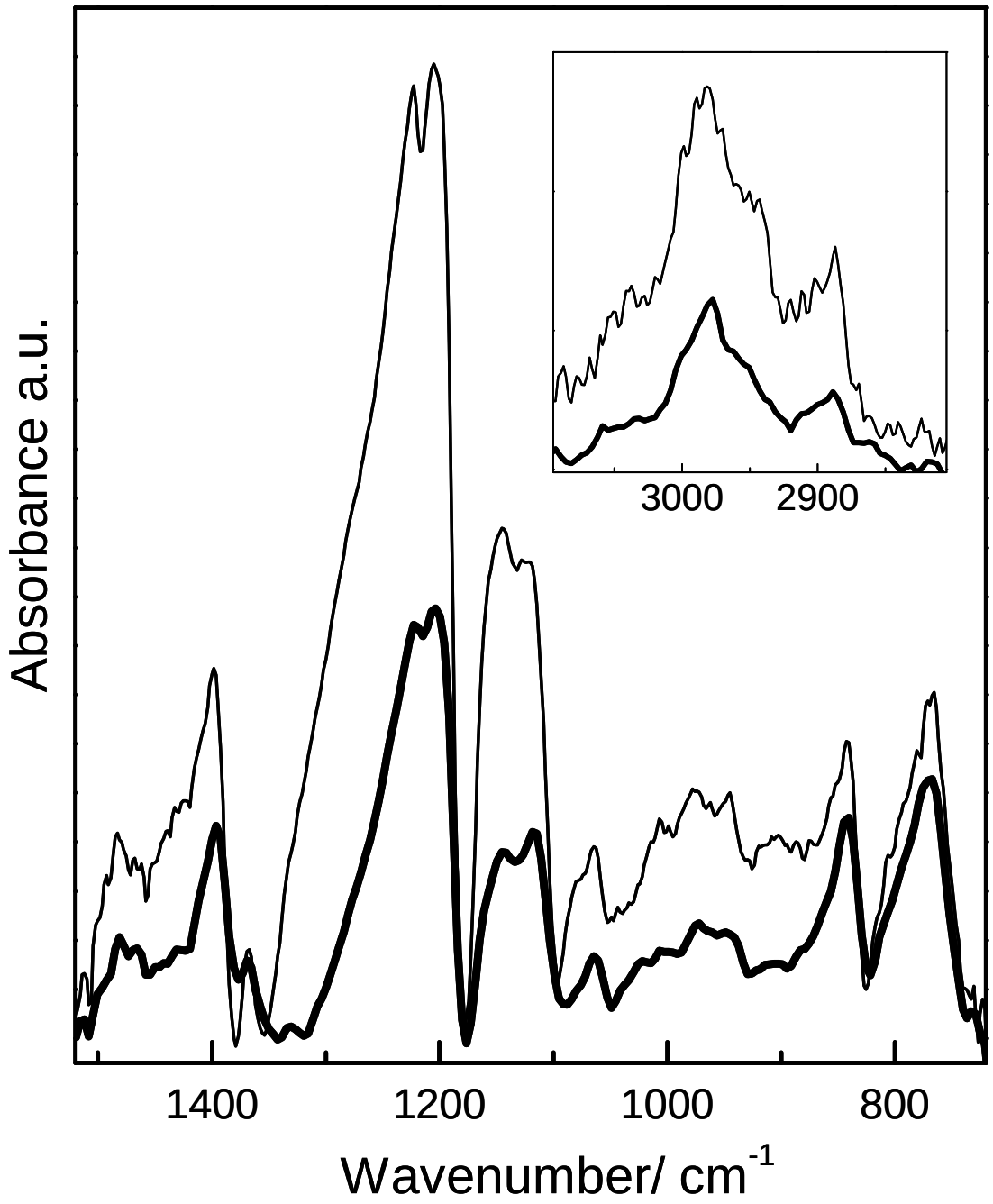

Figure 9: Hardwick et al.